View Synthesis of Dynamic Scenes Based on Deep 3D Mask Volume

Kai-En Lin, Guowei Yang, Lei Xiao, Feng Liu, and Ravi Ramamoorthi, *Fellow, IEEE*

***Abstract*— Image view synthesis has seen great success in reconstructing photorealistic visuals, thanks to deep learning and various novel representations. The next key step in immersive virtual experiences is view synthesis of dynamic scenes. However, several challenges exist due to the lack of high-quality training datasets, and the additional time dimension for videos of dynamic scenes. To address this issue, we introduce a multi-view video dataset, captured with a custom 10-camera rig in 120FPS. The dataset contains 96 high-quality scenes showing various visual effects and human interactions in outdoor scenes. We develop a new algorithm, Deep 3D Mask Volume, which enables temporally-stable view extrapolation from binocular videos of dynamic scenes, captured by static cameras. Our algorithm addresses the temporal inconsistency of disocclusions by identifying the error-prone areas with a 3D mask volume, and replaces them with static background observed throughout the video. Our method enables manipulation in 3D space as opposed to simple 2D masks, We demonstrate better temporal stability than frame-by-frame static view synthesis methods, or those that use 2D masks. The resulting view synthesis videos show minimal flickering artifacts and allow for larger translational movements.**

***Index Terms*—Computer vision, view synthesis.**

I. Introduction

RECENT advances in view synthesis have shown promising results in creating immersive virtual experiences from images. Nonetheless, in order to reconstruct compelling and intimate interaction with the virtual scene, the ability to incorporate temporal information is much needed. In this paper, we study a specific setup where the input videos are from static, binocular cameras and novel views are mostly extrapolated from the input videos, similar to the case in StereoMag [2]. We believe that this case is useful as dual- and multi-camera smartphones are gaining traction and it could also prove to be interesting for 3D teleconferencing, surveillance or playback on virtual reality headsets. Moreover, we can acquire the dataset from a static camera rig as shown in Fig. 1. Although we can apply state-of-the-art image view synthesis algorithms [1], [2], [3], [4] on each individual video frame, the results lack temporal consistency and often show flickering artifacts. The issues mostly come from the unseen occluded regions as the algorithm predicts them on a per-frame basis. The resulting estimations are not consistent across the time dimension, which causes some regions to become unstable when shown in a video.

In this paper, we address the temporal inconsistency when extrapolating views by exploiting the static background information across time. To this end, we employ a 3D mask volume, which allows manipulation in 3D space as opposed to a 2D mask, to reason about moving objects in the scene and reuse static background observations across the video. As shown in Fig. 4, we first promote the instantaneous and background inputs into two sets of multiplane images (MPI) [2] via an MPI network. Then, we warp the same set of input images to create a temporal plane sweep volume, providing information about the 3D structure of the scene. The mask network converts this volume to a 3D mask volume which allows us to blend between the two sets of MPIs. Finally, the blended MPI volume can render novel views with minimal flickering artifacts. To train this network, we also introduce a new multi-view video dataset to address the lack of publicly available data. We build a custom camera rig comprised of 10 action cameras and capture high-quality 120FPS videos with the static rig (see Fig. 1). Our dataset contains 96 dynamic scenes of various outdoor environments and human motions. We show that the proposed method generates temporally stable results against previous state-of-the-art methods, while only using two input views.

Our contributions can be summarized as:

- a multi-view video dataset composed of 96 dynamic scenes (Section III);
- a novel 3D volumetric mask able to segment dynamic objects from static background in 3D, producing higher-quality and temporally stable results than state-of-the-art methods (Section IV-B);
- a synthetic dataset to evaluate complex background (Section V-C);
- experiments including comparison to recent NeRF-based dynamic view synthesis methods (Sections V-B and V-C).

This paper is an extended version of Deep 3D Mask Volume for View Synthesis of Dynamic Scenes [5]. In this journal version, we conduct further experiments to evaluate concurrent

Manuscript received 26 January 2022; revised 7 March 2023; accepted 20 June 2023. Date of publication 26 June 2023; date of current version 3 October 2023. This work was supported in part by a Qualcomm FMA Fellowship, ONR under Grants N000142012529 and N000142312526, in part by the NSF under Grants 2100237 and 2120019, and all awarded to the UCSD researchers. Recommended for acceptance by Y. Furukawa. *(Kai-En Lin and Guowei Yang contributed equally to this work.) (Corresponding author: Guowei Yang.)*

Kai-En Lin, Guowei Yang, and Ravi Ramamoorthi are with the CSE Department, University of California, San Diego, La Jolla, CA 92037 USA (e-mail: k2lin@eng.ucsd.edu; g4yang@ucsd.edu; ravir@cs.ucsd.edu).

Lei Xiao is with Reality Labs Research, Meta, Redmond, WA 98052 USA (e-mail: lei.xiao@fb.com).

Feng Liu is with Computer Science Department, Portland State University, Portland, OR 97207 USA (e-mail: fliu@cs.pdx.edu).

This article has supplementary downloadable material available at https://doi.org/10.1109/TPAMI.2023.3289333, provided by the authors.

Digital Object Identifier 10.1109/TPAMI.2023.3289333

Fig. 1. Our custom camera rig. Top left figure shows the configuration we use for evaluation in Section V. We show the input stereo image sequences from camera 4 and camera 5 in the middle. The rightmost column shows the crops of rendered novel view at camera 0. Artifacts appear when the novel view is translated by a larger distance. We use the conventional MPI method [1] as our baseline algorithm. Note how the area on top of the person's head is distorted and shows "stack of cards" artifacts. This type of artifact flickers in a dynamic video as the network hallucinates the disocclusion per-frame.

NeRF-based methods [6], [7], [8] in Section V-B. These methods target a monocular dynamic camera setup different from our static stereo camera setup. A moving monocular camera effectively provides multiple viewpoints of the static scene components. On the contrary, static stereo cameras can only supply two viewpoints and thus their methods do not perform as well as our proposed method. To show experiments in a more controlled environment and allow for more complex backgrounds, we created a new synthetic dataset to evaluate the performance in Section V-C. We demonstrate how our method can tackle the dynamic background with multiple actors. Moreover, we detail how different loss functions would affect the visual results in Section V-D, as well as large distance view extrapolation in Section V-E and extension to more input views in Section V-F.

II. Related Work

Our goal is to achieve temporally stable view synthesis on dynamic scenes. We are inspired by several previous methods in view synthesis and space-time synthesis.

A. View Synthesis

View synthesis is a complicated problem which has become a popular field of research in computer vision and graphics. Earlier lines of work utilize dense sampling from the scene to create light fields [17], [18]. Image-based rendering techniques [19], [20] exploit proxy geometry of the scene to produce novel view renderings. Later extensions on this topic introduce better modeling of the scene structure [21] and hand-crafted heuristics [22], [23]. As deep learning became dominant, learning-based methods [24], [25], [26], [27], [28] have shown promising results. Recently, a class of research works focuses on combining novel representations [1], [2], [3], [9], [29], [30], [31], [32], [33], [34] with a differentiable rendering pipeline to produce high-quality results. Another exciting advance is neural radiance fields (NeRF) [29], which encodes the 3D scene structure in a compact continuous 5D volumetric function. Although NeRF has shown promising view synthesis results, it has to overfit to the given scene with enough samples (10 or more), requiring time-consuming per-scene training. Rendering time could take up to 30 s for one image, whereas our pipeline allows inference and rendering in less than 2 s without dedicated optimization, using only binocular input views. Instead, in this paper we focus on a specific layered representation, multiplane images (MPI) [1], [2], [3], [10], [35], as it provides good generalizability across various scenes and efficiency capable of real-time rendering. Our proposed method directly tackles the temporal instability introduced in MPIs when the disoccluded areas lead to different estimations across time.

B. Space-Time Synthesis

Space-time synthesis is a more complicated problem since it not only involves movement of the novel viewpoint in space, but also incorporates differences of time. A body of work covers appearance changes such as relighting while changing views [27], [36], [37], [38], [39]. However, these methods focus on the lighting change with respect to a static scene, treating dynamic objects in the scene as outliers. On the other hand, some methods directly target dynamic scenes [10], [11], [13], [15], [40]. While our method utilizes MPIs similar to Broxton et al. [10], they employ dense sampling of 46 cameras to reconstruct light fields of the viewing volume, essentially interpolating between cameras. Our method focuses on the stereo case similar to StereoMag [2], targeting extrapolation from stereo inputs like dual-camera smartphones. In addition, unlike depth-based methods [11], [13], we do not require any explicit depth maps to render novel viewpoints. As depth-based methods often yield flickering and require hole-filling, we instead use a representation more suitable for rendering. Another issue that these methods do not address is the lack of generalizability. Bansal et al. [13] is trained on limited data which could make the learned network overfit to a small number of scenes. Moreover, while Yoon et al. [11] uses a pretrained network to ensure generalizability on unseen scenes, it still requires human-generated masks for foreground and background separation. We capture various

TABLE I
COMPARISON OF DIFFERENT MULTI-VIEW DATASETS

Dataset	Scene count	Rigid rig	Large disparity	Views	Dynamic	Public	Remarks
Real Forward-Facing [1]	65	✗	✓	25	✗	✗	Loosely gridlike formation
Spaces [9]	100	✓	✓	16	✗	✓	Strictly gridlike formation
Immersive LF Video [10]	130	✓	✓	46	✓	✗	Spherical formation
Dynamic Scene [11]	8	✓	✓	12	✓	✓	Few temporal frames
Single Image LF [12]	∼2000	✓	✗	196	✗	✓	Small baseline light fields
RealEstate10K [2]	∼10000	✗	✓	1	✗	✓	Static scenes
Open4D [13]	6	✗	✓	15	✓	✓	Free-viewpoint capture
MannequinChallenge [14]	∼2000	✗	✓	1	✗	✓	Mostly static scenes
X-Fields [15]	8	✓	✓	5	✓	✓	Few temporal frames
KITTI [16]	400	✓	✓	2	✓	✓	Binocular setup on cars
Ours	96	✓	✓	10	✓	✓	Publicly released

dynamic scenes with human interactions to train our network and ensure that it is generalizable across different unseen scenes. Also, our network utilizes the background information extracted from video and uses it to directly segment the foreground and background in 3D space without any human input.

Concurrently, there are several NeRF-based algorithms [6], [7], [8] which demonstrate state-of-the-art performance on monocular video inputs with a moving camera. For static parts of the scene, a moving camera provides multi-view cues to the network and they can be reconstructed in the same process as the original NeRF [29]. For dynamic parts of the scene, NSFF [7] learns an implicit representation of the scene flow and warps the sampled points to render the scene at different timesteps. Similarly, NeRFlow [6] also uses an MLP network to learn the underlying scene flow but it incorporates a neural ODE to enforce consistency across continuous time. Non-rigid NeRF [8] optimizes for a canonical volume model, then it uses deformation fields to generate renderings at different timestamps. Although these methods work well for a single moving camera, they are not able to acquire good 3D geometry for a pair of static cameras. As demonstrated in Section V-B, our MPI-based method is able to utilize better geometry priors to provide high-quality results during extrapolation with less distortion and flickering.

III. DATASET

High-quality video datasets are crucial for learning-based novel-view video synthesis algorithms. The ideal datasets would contain a diversity of scenes, captured at multiple synchronized views. In this work we introduce a novel multi-view video dataset. We discuss the limitations of existing datasets compared to our dataset in Section III-A. We describe our data capture and generation process in Section III-B. Finally, we discuss the statistics and advanced properties of our dataset in Section III-C.

A. Multi-View Video Dataset

As shown in Table I, we evaluate several properties which are important to train a generalized view synthesis network. Specifically, a rigid camera rig is preferred as it can provide good pose priors and ensure the accuracy of the estimated camera poses. On the contrary, unstructured captures like Real Forward-Facing [1] and Open4D [13] do not use pose priors and utilize structure from motion, which could produce varying accuracy depending on scene geometry and the texture presented. In addition, rigid camera rigs allow for capture of dynamic scenes with multiple simultaneous camera views. On account of the above reasons, our dataset is captured with a custom camera rig that is rigid and robust enough to offer good pose priors.

Number of views is also an important factor for a multi-view dataset since different combinations of input and target camera pairs provide diversity in baselines and camera motions. X-Fields [15] and KITTI [16] provide limited views and camera motions and thus are not as useful for video view synthesis tasks. Our dataset offers 10 different camera views in a gridlike formation (see Fig. 1). For our binocular view synthesis task, we choose 2 views out of 10 and 1 from the rest to construct a training pair. The most important feature is to have enough temporal frames and dynamic movements for training. Most datasets fail at this part as they target the image view synthesis task instead of a video one. Although the Dynamic Scene Dataset presented by Yoon et al. [11] targets the dynamic scenes, it uses frame skips to keep salient movements. Thus, the movements shown in the dataset are not smooth and fail to provide enough training samples. To address this issue, our dataset is captured in 120 FPS and synchronized as a post-process (see Section III-B), making it easy to perform and evaluate view synthesis at different framerates.

One dataset that targets the purpose of video view synthesis is the Immersive Light Field Video dataset proposed by Broxton et al. [10], which contains 46 camera views and 130 different dynamic scenes. However, the full dataset is not publicly available to the community. Our full dataset can be found at http://cseweb.ucsd.edu/%7eviscomp/projects/ICCV21Deep/

B. Dataset Generation

Our video dataset is captured with a custom camera rig that consists of 10 GoPro Hero 7 Black action cameras as shown in Fig. 1. The horizontal baseline between neighbor cameras is approximately 10 cm and the vertical distance between rows is around 14 cm. We captured 96 outdoor videos in 120 FPS,

Fig. 2. Digital clock and the randomly moving QR code pattern used to perform synchronization. We have two ways to do synchronization: (1) matching the timestamp; (2) aligning the QR code location in all views. We use these methods to ensure the synchronization is accurate enough.

TABLE II
NUMBER OF VIDEOS THAT CONTAIN EACH OCCLUSION TYPE AS DESCRIBED IN SECTION III-C

Occlusion types	(a)	(b)	(c)	(d)	Total videos
Count	90	96	42	19	96

Note that most scenes typically contain multiple types of occlusion.

with the camera rig being static for each video. As GoPros only allow fisheye mode for high FPS captures, we calibrate the cameras with a 17x14 checkerboard pattern (squares have side lengths of 40 mm) and undistort the videos using a pinhole camera model [41] implemented in OpenCV [42]. For camera extrinsics, we choose the first frame from all views as inputs to COLMAP [43], [44], which then does feature extraction, feature matching, and sparse reconstruction. The reconstructed camera poses are assumed to be fixed for the duration of each video. In addition, to achieve synchronization, we display a digital clock with randomly appearing QR code patterns (see Fig. 2) on a high refresh rate screen that can be seen by all cameras at the same time. Then, we manually edit and align the multi-view videos according to the digital clock and QR code pattern.

C. Dataset Statistics

Our videos are mostly around 1 to 2 minutes long and all videos are shot in 120 FPS. We cover different scenes to ensure that the surface reflectance variety is high enough. For example, in Fig. 3 we show that in our dataset we cover different buildings, furniture, foliage and specularity effects. Another important aspect of our dataset is the inclusion of different human motions, including slower motions like walking, sitting down and faster motions, such as running, jumping and arms waving. We now discuss four possible types of occlusion interactions and show the numbers of their occurrences in Table II.

a) Static Occluder and Static Background. For example, the table in Fig. 3(c) occludes the areas behind. Most view synthesis methods target this case as this is one of the most common cases. We describe it as a static occluder in the scene blocking the line-of-sight from the cameras to the background scene. Background information can only be acquired from the views with direct line-of-sight. As such, it is difficult to recover the unseen regions without prior knowledge of the scene. However, temporal consistency in these areas is easily achievable because inputs remain relatively unchanged throughout the video. Hallucination of the disoccluded areas can also remain the same for this case.

b) Dynamic Occluder and Static Background: Another type of event happens when a dynamic object is moving across the scene. For example, the person in Fig. 3(a) and (e) walks in front of the static background. In these scenes, the camera has line-of-sight on the background behind the person at some point in the video. Therefore, it is relatively easy to acquire static background information as the occluder does not block the line-of-sight in all video frames. Combining information from multiple frames throughout the video provides an accurate rendering of what is behind the dynamic occluder. Temporal consistency in this case can also be maintained by substituting the static background for the dynamically-occluded regions. In other words, we can perform hole-filling based on the observations from other video frames. Our proposed method takes advantage of this prior knowledge to generate temporally-stable view synthesis results, as opposed to previous methods.

c) Static Occluder and Dynamic Background: This case happens when an object moves behind a static occluder and thus the camera does not have full visuals on it. For example, the person walks behind a traffic sign in Fig. 3(f). In this case as it is only a short-term occlusion, the person's appearance can be interpolated between different frames. However, in the case of a larger wall, this becomes difficult to solve as extrapolating the movement is complicated and the ambiguity could lead to different outcomes. In general, it is difficult to accurately predict the trajectory of the occluded object without assuming it is moving at constant velocity. For temporal consistency, the movement of dynamic objects can lead to instability of the novel view prediction. Our method learns to detect the dynamic movements and treat the static part of the scene as (a) such that flickering artifacts are kept at a minimal level.

d) Dynamic Occluder and Dynamic Background: The last case happens when the occluder and the background object are both moving or the background appearance is changing. For instance, two people walk towards each other parallel to the camera's image plane in Fig. 3(g). Similar to (c), how the occluded object is moving remains ambiguous and hard to resolve deterministically. Although we do not have a clear idea of the occluded parts, we can still ensure it is temporally stable when shown. We can reduce this case to (b) with the ambiguity that the occluded object can move anywhere. And as a result, the occluded regions look more or less similar to the static background.

Our dataset contains diverse occlusion interactions and we show results in Section V-B and provide an analysis in Fig. 6.

IV. DEEP 3D MASK VOLUME

Our goal is to synthesize temporally consistent novel view videos given stereo video inputs. Consequently, we build our algorithm upon prior work on multiplane images [1], [2] and propose a novel mask volume structure to fully utilize the temporal background information and the layered representation.

Fig. 3. A selection of still frames from our dataset. We captured various dynamic scenes with human motions, including walking, running, jumping, and sitting down. Note that cameras remain static for the whole duration of the capture.

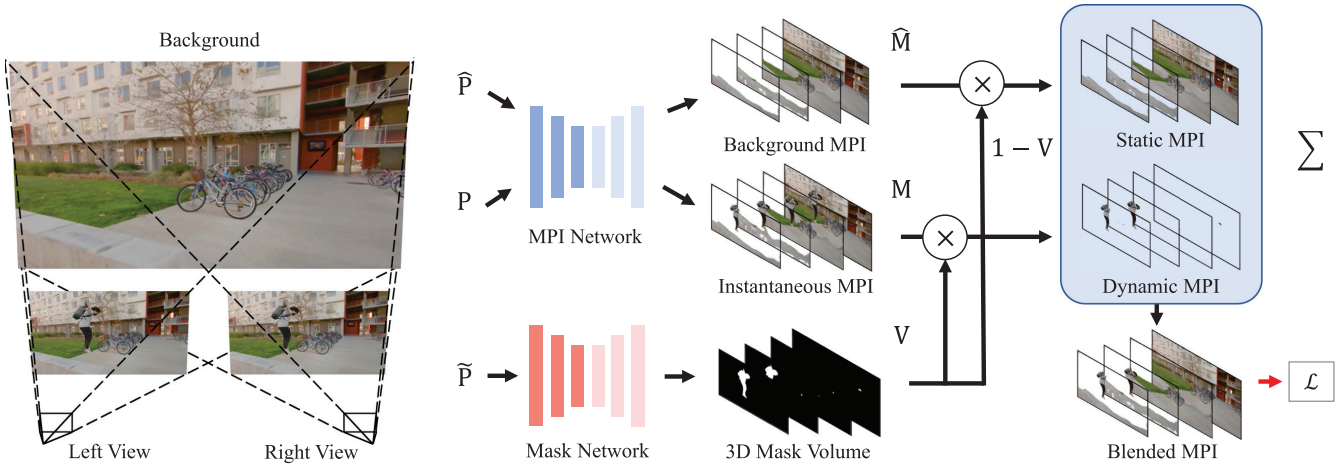

Fig. 4. Overview of our pipeline. Given binocular input videos, our MPI network promotes the 2D multiview images to two 3D MPI representations; one encodes the instantaneous information and the other encodes the background information. The mask network produces a 3D mask volume $\mathbf{V}$ to modulate the MPIs and blend them together, producing the final output. Please see Section IV-B for more details.

In this section, we start with a brief review of the multiplane images in Section IV-A. Then we describe our 3D mask volume in Section IV-B. Finally we discuss our loss function design in Section IV-D. Please refer to Fig. 4 for an overview of our algorithm pipeline.

A. Multiplane Images

Our approach takes inspiration from recent advancements in multiplane image representation [2], [45]. Multiplane images (MPI) are a layered representation of the 3D scene. They consist of D layers of RGBα images, representing the viewing frustum from the perspective of a virtual reference camera. The planes partition the viewing frustum according to equally-spaced disparity (inverse depth) values $d_0, d_1, \ldots, d_{D-1}$. Each layer of the MPI encodes color C and transparency information α at a specified plane depth d. We denote the MPI layer at disparity d as a tuple of (C_d, α_d). To construct such a volume, we warp input views to the reference camera position (in our case, the center left camera, numbered 4 in the camera rig diagram in Fig. 1) to construct a plane sweep volume (PSV). The PSV is then used as the input to a 3D CNN similar to the one used by Mildenhall et al. [1] and it generates the corresponding MPI volume. To render a novel viewpoint j from camera i, the MPI layers are warped using planar homography as follows:

$$\mathcal{W}^d_{i\to j}(C_d, \alpha_d), \tag{1}$$

where $\mathcal{W}$ is the warping operator. The warped MPIs are then composited with the over operation. To be more specific, we calculate the per-pixel transmittance t from the alpha value at location (x, y) on plane d by

$$t(x, y, d) = \alpha(x, y, d) \prod_{d'>d} [1 - \alpha(x, y, d')]. \tag{2}$$

The final rendering at each pixel C_{final} is computed as

$$C_{final}(x, y) = \sum_d C(x, y, d) t(x, y, d). \tag{3}$$

These computations are parallelizable and their efficiency during rendering makes the MPI a good representation for fast view synthesis.

One observation of MPIs is that the unseen parts in the volume are often merely repeated texture of the foreground objects [3]. This happens when the input camera baseline is not large enough and the resulting PSV cannot provide further information about the background. In addition, these areas typically present different estimations between frames. Therefore, the unseen areas produce visible artifacts, especially in video view synthesis (see Fig. 1). On the other hand, visible parts usually provide temporally stable results as can be seen in Broxton et al. [10]

B. 3D Mask Volume Generation

From Section IV-A, we observe that most artifacts are introduced by the disocclusion of moving objects. In order to address this issue, we seek to find a 3D mask volume that identifies the dynamic components and removes the flickering artifacts behind them accordingly. To be more specific, given a pair of stereo image sequences of length n, $\{\mathbf{I}_0^L, \mathbf{I}_1^L, \ldots, \mathbf{I}_{n-1}^L\}$ and $\{\mathbf{I}_0^R, \mathbf{I}_1^R, \ldots, \mathbf{I}_{n-1}^R\}$, we wish to derive a 3D mask $\mathbf{V}(x, y, d)$, such that

$$\mathbf{V}(x,y,d) = \begin{cases} 1, & \text{if } \mathbf{I}(x,y) \neq \hat{\mathbf{I}}(x,y), d > \mathbf{D}(x,y) \\ 0, & \text{otherwise} \end{cases}, \quad (4)$$

where $\mathbf{I}$ is the instantaneous frame, $\hat{\mathbf{I}}$ denotes the background image, and $\mathbf{D}$ is the scene disparity observed by the camera. We drop the frame subscript as a shorthand for instantaneous frame in the following discussion. In addition, we represent the instantaneous MPI of the scene as $\mathbf{M}(x, y, d)$, and the background MPI as $\hat{\mathbf{M}}(x, y, d)$.

The main purpose of the 3D mask volume $\mathbf{V}(x, y, d)$ is to partition the scene $\mathbf{M}(x, y, d)$ into two parts: static and dynamic. The static portion of the MPI does not change for the whole video duration, and thus $\mathbf{M}(x, y, d) = \hat{\mathbf{M}}(x, y, d)$, when $\mathbf{V}(x, y, d) = 0$. The synthesized novel view of these parts is temporally stable and requires no further modification to the algorithm. On the contrary, the dynamic objects ($\mathbf{V}(x, y, d) = 1$) could move in different directions. The disoccluded areas, given mathematically by $\mathbf{M}(x, y, d)$ if $\mathbf{I}(x, y) \neq \hat{\mathbf{I}}(x, y), d > \mathbf{D}(x, y)$, often change with them, producing "stack of card" artifacts and flickering when viewed from another angle (see Fig. 1). However these areas in fact usually resemble the background $\hat{\mathbf{I}}$. With this knowledge, a clear separation between the static and dynamic scene components allows us to identify the disocclusion and minimize the temporal inconsistency by

$$\mathbf{M}(x,y,d) \leftarrow \hat{\mathbf{M}}(x,y,d) \text{ if } \mathbf{I}(x,y) \neq \hat{\mathbf{I}}(x,y), d < \mathbf{D}(x,y). \quad (5)$$

Essentially, we are using the temporally-stable static background to replace the unknown disoccluded areas. An illustration of the mask is given in Fig. 4. In order to perform the operation in (5), our network is composed of two networks: *MPI network* generates 2 layered representations of the 3D scene, namely $\mathbf{M}(x, y, d)$ and $\hat{\mathbf{M}}(x, y, d)$; *Mask network* produces the 3D mask volume $\mathbf{V}(x, y, d)$ satisfying (4). We show each network in Fig. 4 and discuss them in details as follows:

MPI Network. It is necessary to acquire 3D information from both the instantaneous frame and throughout the whole video, so we can then obtain the needed information behind the dynamic occluder. To this end, we first apply a median filter $\mathcal{A}$ on the image sequences

$$\hat{\mathbf{I}} = \mathcal{A}(\{\mathbf{I}_0, \mathbf{I}_1, \ldots, \mathbf{I}_{n-1}\}). \quad (6)$$

It is applied to both views to generate the corresponding background images.

Then, we can inversely warp $\mathbf{I}^R$ and $\hat{\mathbf{I}}^R$ to the left camera and construct a PSV. The PSV from the instantaneous frame is generated as

$$\mathbf{P} = \{\mathbf{I}^L, \mathcal{W}_{R\to L}^{d_0}(\mathbf{I}^R), \mathcal{W}_{R\to L}^{d_1}(\mathbf{I}^R), \ldots, \mathcal{W}_{R\to L}^{d_{D-1}}(\mathbf{I}^R)\}. \quad (7)$$

It is then used as an input to a 3D CNN $\mathcal{F}_\theta$ to produce the instantaneous MPI, $\mathbf{M} = \mathcal{F}_\theta(\mathbf{P})$. Similarly, we construct the background MPI, $\hat{\mathbf{M}}$, using another PSV, $\hat{\mathbf{P}}$, generated from $\hat{\mathbf{I}}^L$ and $\hat{\mathbf{I}}^R$. The two MPIs, $\mathbf{M}$ and $\hat{\mathbf{M}}$, now contain the information of the dynamic occluder and the static background.

Mask Network. We utilize another 3D CNN $\mathcal{G}_\theta$ to reason about the relationship between the MPIs and generate a mask volume $\mathbf{V}$ to satisfy (4). Inspired by background matting [46] on 2D images, our mask network takes a similar approach but in 3D space. From (6), we define a temporal plane sweep volume (TPSV) as follows

$$\begin{aligned}\tilde{\mathbf{P}} = \{&\mathbf{I}^L, \mathcal{W}_{R\to L}^{d_0}(\mathbf{I}^R), \ldots, \mathcal{W}_{R\to L}^{d_{D-1}}(\mathbf{I}^R), \\ &\hat{\mathbf{I}}^L, \mathcal{W}_{R\to L}^{d_0}(\hat{\mathbf{I}}^R), \ldots, \mathcal{W}_{R\to L}^{d_{D-1}}(\hat{\mathbf{I}}^R)\}. \end{aligned} \quad (8)$$

The TPSV helps the network to distinguish the dynamically-occluded parts in the 3D scene. Then, we acquire the 3D mask volume by $\mathbf{V} = \mathcal{G}_\theta(\tilde{\mathbf{P}})$.

Finally, we can calculate the final MPI $\mathbf{M}_o$ by

$$\begin{aligned}\mathbf{M}_o(x,y,d) = &\mathbf{M}(x,y,d)\mathbf{V}(x,y,d) \\ &+ \hat{\mathbf{M}}(x,y,d)(1 - \mathbf{V}(x,y,d)), \end{aligned} \quad (9)$$

for all (x, y, d). We define a shorthand version as

$$\mathbf{M}_o = \mathbf{M} \odot \mathbf{V} + \hat{\mathbf{M}} \odot (1 - \mathbf{V}), \quad (10)$$

where $\odot$ means element-wise multiplication. $\mathbf{M}_o$ achieves (5) as our learnable mask volume $\mathbf{V}$ satisfies (4) and we can then render the output image $\mathbf{I}_o$ using planar homography and the over composite operation described in Section IV-A. Please refer to Fig. 4 for illustrations.

One major difference between using a 3D mask volume $\mathbf{V}(x, y, d)$ and a 2D mask $\mathbf{V}'(x, y)$ is that the former is able to segment out the dynamic objects in the 3D space, namely (4) and subsequently do (5). In Fig. 4, notice that the mask volume only contains the dynamic object (jumping person in this case). In contrast, a 2D mask $\mathbf{V}'(x, y)$ does not vary with respect to the disparity d, making it impossible to manipulate the areas behind dynamic objects.

TABLE III
DETAILS OF EACH LAYER IN OUR 3D MASK NETWORK

Layer	kernel size	stride	dilation	in	out	activation	input
conv1_1	7	1	1	12	8	ReLU	PSVs
conv1_2	7	2	1	8	16	ReLU	conv1_1
conv2_1	3	1	1	16	16	ReLU	conv1_2
conv2_2	3	2	1	16	32	ReLU	conv2_1
conv3_1	3	1	1	32	32	ReLU	conv2_2
conv3_2	3	2	1	32	64	ReLU	conv3_1
conv4_1	3	1	1	64	64	ReLU	conv3_2
conv4_2	3	1	1	64	64	ReLU	conv4_1
up5	-	2	-	128	128	-	conv3_2 + conv4_2
conv5_1	3	1	1	128	32	ReLU	nnup5
conv5_2	3	1	1	32	32	ReLU	conv5_1
up6	-	2	-	64	64	-	conv2_2 + conv5_2
conv6_1	3	1	1	64	16	ReLU	nnup6
conv6_2	3	1	1	16	16	ReLU	conv6_1
up7	-	2	-	32	32	-	conv1_1 + conv6_2
conv7_1	3	1	1	32	16	ReLU	nnup7
conv7_2	3	1	1	16	8	ReLU	conv7_1
conv7_3	3	1	1	8	1	Sigmoid	conv7_2

C. Network Architecture

Our view synthesis pipeline utilizes two different 3D CNNs to predict the MPI volumes and the 3D mask volume as described in Section IV-B. Both networks have similar structures as the one in Mildenhall et al. [1]. However, we made some adjustments to keep the network light for faster training and less memory consumption. We show detailed layers for the mask network in Table III. The MPI network has the same structure except for some changes in the overall input and output channels to account for different view counts.

D. Loss Function

We implement our loss function as a rendering loss, similar to previous work on MPIs [1], [2], [3]. For the rendering loss, we use view synthesis as the supervision task and let the algorithm render a held-out view from the final MPI $\mathbf{M}_o$ (see Fig. 4). The rendering loss is as follows:

$$\mathcal{L} = \frac{||\mathcal{F}_{VGG}(\mathbf{I}_o) - \mathcal{F}_{VGG}(\mathbf{I}_{gt})||_1}{N}, \tag{11}$$

where $\mathcal{F}_{VGG}$ is the VGG-19 network [47], N is the number of elements in the image $\mathbf{I}_o$, and $\mathbf{I}_{gt}$ is the held-out ground truth view. This perceptual loss is similar to the implementation of Chen et al. [48]. We also considered a mask supervision loss $\mathcal{L}_m$ and a mask sparsity constraint $\mathcal{L}_s$. However, we did not find them to be useful for temporal consistency. Ablation studies on these two losses can be found later in Table VI, and details are in Section V-D.

V. RESULTS

In this section, we discuss implementation details for our network in Section V-A. Then we show comparisons to other methods on our dataset in Section V-B. We include comparisons on our synthetic dataset in Section V-C. To explore the effects of different loss functions, we show the ablation studies in Section V-D. We show that our method is able to degrade gracefully even doing view extrapolation far outside the viewing volume in Section V-E. Our method can also be extended to incorporate more input views in Section V-F. Finally we discuss limitations of our current setup and method in Section V-G. Result videos can be found in the supplementary materials, available online.

A. Implementation Details

Due to GPU memory constraints, we choose a two-step training scheme to train our network. We first train the MPI network on the RealEstate10 K dataset [2], and then train only the mask network on our own video dataset. This training scheme can keep the memory usage within a reasonable range and the speed fast enough.

The MPI generation network is trained by predicting a held-out novel view and applying the rendering loss $\mathcal{L}$ as supervision. This stage is trained for 800 K steps. After the previous pretraining stage, we freeze the weights of the MPI network and train only the mask network using the loss $\mathcal{L}$. The network takes 2 random views from the 10 views as input and we randomly choose a target camera position from the rest of the views at each step. We select 86 out of the 96 scenes as our training dataset and images are rescaled to 640×360. This second stage is trained for 100 K steps. The learning rate is set to $5e-4$ for both stages. Our training pipeline is implemented in PyTorch [50] and training takes around 5 days on a single RTX 2080Ti GPU. With resolution in 640×360, inferencing $\mathbf{M}_o$ using our full pipeline takes around 1.75 s, while rendering takes another 0.28 s. Note that the rendering pipeline is implemented in PyTorch without further optimization. In practice, it could be significantly faster with OpenGL or other rasterizer.

B. Comparisons on Real Data

For comparison, we choose 7 unseen videos from the dataset and subdivide them into 14 clips, focusing on salient movements in the scene. The methods we chose to evaluate includes MPI-based methods like LLFF, and also emerging NeRF-based methods like Nonrigid-NeRF, Neural Scene Flow Field, and NeRFlow We ran all methods on the clips with camera 4 and 5 as input and others as the target output (see Fig. 1). Error metrics are calculated between the output and the ground truth images. For monocular NeRF-based methods [6], [7], [8], as they assume the input to be monocular, moving camera, and have increasing time steps, we alternate between left and right views to satisfy this assumption. This allows the algorithm to treat the input as a monocular video with the camera jumping between two viewpoints.

We compare with 6 baseline approaches: (1) MPI/LLFF is our adaptation of Mildenhall et al. [1] to work with only two input views and different camera intrinsics. It processes the stereo input videos and renders the novel view frames on a per-frame basis. We trained it on the same dataset as our method. (2) 2D mask is our naive baseline method, which is similar to our pipeline, except that it uses a foreground mask $\mathbf{V}'(x, y)$ generated by the background matting method [46] with $\mathbf{I}$ and $\hat{\mathbf{I}}$ as inputs. The blended MPI $\mathbf{M}'_o$ for (2) is obtained by

$$\mathbf{M}'_o = \mathbf{V}'(x, y) \odot \mathbf{M} + (1 - \mathbf{V}'(x, y)) \odot \hat{\mathbf{M}},$$

where the 2D mask has been expanded into 3D by repeating its values along the depth dimension. (3) IBRNet [49] uses the

TABLE IV
COMPARISON ON OUR EVALUATION DATASET

Methods	Mask	STRRED↓	PSNR↑	SSIM↑
MPI/LLFF [1]	✗	0.2917	25.52	0.8227
2D Mask	2D	0.2892	25.50	0.8242
IBRNet (2-view) [49]	✗	2.2606	21.49	0.6713
NeRFlow [6]	✗	3.2646	16.81	0.4146
NSFF [7]	✗	1.4230	17.04	0.4197
Non-rigid NeRF [8]	✗	2.3941	18.11	0.4997
Ours	3D	**0.1683**	**26.22**	**0.8390**

We compare with different baseline methods and the results show that our 3D mask offers much better temporal stability. 2D mask does not improve much because it fails to resolve the ambiguity in disoccluded areas.

official implementation and their pretrained model weights, and it takes 2 views as input on a per-frame basis. (4) NeRFlow [6] uses the official implementation and we slightly modify the necessary parts to allow for two alternating views as input. (5) NSFF [7] is also adapted from the official implementation to take two input views. (6) Non-rigid NeRF [8] uses the released official implementation with modifications to enable two-view inputs. For (4)-(6), we train them for 20,000 steps for each scene and render the corresponding viewpoints. Please refer to our supplementary materials for the video results, available online.

From Table IV, we see that our method is able to achieve temporally-coherent rendering, while offering better visual quality and fewer distortions. Specifically, we employ the STRRED metric [51] to evaluate stability across time. Our method significantly reduces the temporal artifacts across most scenes while also keeping PSNR and SSIM better than the baseline methods. For MPI/LLFF, since it does not utilize the information across the whole video, it yields more flickering and distorted areas as can be seen in Fig. 5. For example, in the top scene, there is a ghosting artifact around the person's head and it changes frame-by-frame, resulting in flickering video. The 2D mask method is a binary mask that naively selects the dynamic parts in $\mathbf{M}$ and the background in $\hat{\mathbf{M}}$ to produce the final MPI. As a result, it amplifies the stack of cards artifacts (see Fig. 5) and also slightly worsens the visual quality as shown in Table IV. IBRNet [49], does not work well with 2-view input and it produces poor results compared to ours. Concurrent monocular NeRF-based methods [6], [7], [8] perform similarly in Table IV. With only two input viewpoints, they fail to represent even the static scene components since there are not enough multi-view cues for reconstruction. For dynamic parts of the scene, NSFF provides more stable quality as can be seen from the STRRED metric. In general, our proposed method provides state-of-the-art performance over other previous and concurrent work. We show qualitative results in Fig. 5. Each inset column corresponds to a scene as shown on the leftmost side. We show the MPI baseline method in row (a) and 2D mask baseline in row (b). These two methods suffer from stack-of-card artifacts in particular in the disoccluded regions. 2D mask fails to solve the problem and sometimes makes it more apparent. This is because 2D mask does not reason about the 3D geometry of the scene. For the more recent NeRF-based methods, we show them in row (c-f). NeRFlow [6] provides better static scene reconstruction than other methods. However, it produces blurred results and lacks high-frequency details as can be seen from the second image in row (c). On the other hand, our proposed method is able to make the text on the person more legible and sharper, while suffering little to no disocclusion artifacts. Non-rigid NeRF [8] suffers from significant artifacts when rendering the images. This is possibly due to sparse viewpoints and the network is trying to compensate with deformation fields. NSFF [7] generates sharper images than NeRFlow, but it suffers from blurriness in static parts of the scene. IBRNet [49] produces noisy results given two input views on a frame-by-frame basis. Their method tries to blend different viewpoints with a ray transformer to synthesize disoccluded regions. However, given two input views, this becomes even more difficult because of the lack of samples.

To further analyze how temporal consistency is affected, we characterize the clips with different properties including different types of occlusion discussed in Section III-C and show the results in Fig. 6. As stated earlier, several clips are selected from the 7 scenes to show salient motions. We only include results from MPI/LLFF [1], 2D mask and Ours, as other methods have significantly higher STRRED. From the results, we observe that faster movements could often result in worse temporal consistency, like the differences between clip 1-1 and 1-2. There is an interesting failure in 4-2 for the 2D mask method. 4-1 is the jumping scene in Fig. 5, and 4-2 shows a person walking in the same scene. Although the movement is slower, the person walks past several areas with large appearance changes in 4-2. As a result, the artifacts in the 2D mask are much more obvious, and the video flickers more than other methods, leading to a worse STRRED score.

C. Comparisons on Synthetic Data

In addition to real data, we also crafted a synthetic dataset and tested different methods on it. The synthetic dataset not only can provide us real ground truth to make proper comparisons, but also can illustrate scenes and movements hard to capture in real life, for example, complex moving backgrounds. The synthetic dataset is constructed using scenes from the Habitat-Matterport 3D dataset [52] and UE4 Sun Temple [53], and the moving characters in the scene are pre-animated characters from Adobe Mixamo. We used Blender [54] to composite the scenes, and replicated the 10-view camera array with parameters similar to our GoPro setup. We deliberately set all the cameras to have the same camera intrinsics in order to reduce unwanted artifacts.

For each scene, we rendered 60 frames of the animation, and produced camera poses for all 10 cameras. As all the camera poses can be directly obtained from Blender, we do not need COLMAP [43], [44] to estimate camera poses anymore. The background images are still obtained using median filter. Similar to our evaluation on the real dataset, we chose cameras 4 and 5 as input. In Table V, we show the numbers of various methods. The proposed method achieves favorable results compared to other baselines. Additionally, we show qualitative results in

Fig. 5. We show visual results on 4 different scenes. These scenes include both fast and slow movements, such as waving, jumping and walking. The novel viewpoint is an extrapolation from the input camera views. In the above images, each row is rendered using one method from (a) MPI/LLFF [1], (b) 2D Mask, (c) NeRFlow [6], (d) Non-rigid NeRF [8], (e) Neural Scene Flow Field [7], (f) IBRNet [49], and (g) ours. Last row (h) is the ground truth. Our proposed method produces results with fewer artifacts and more temporal stability.

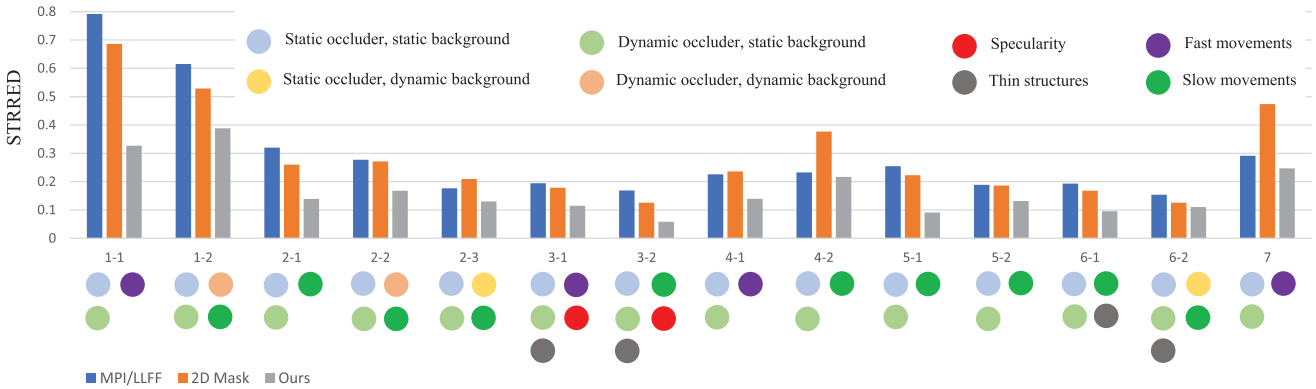

Fig. 6. STRRED comparison on our dataset with baseline methods. We select 14 clips from 7 different scenes. 1-1, 1-2 denotes clip 1 and clip 2 from scene 1.

Fig. 7. For MPI/LLFF, the numbers are slightly worse than our proposed algorithm, because the main difference is in the disoccluded regions. It can be seen in the row (a) around the moving characters. 2D mask introduces more artifacts and thus results in worse numbers across all metrics. In row (b), 2D mask exacerbates the artifacts and creates more visible repeated texture in the disoccluded regions. NeRF-based methods perform slightly better on the synthetic dataset, as the camera parameters are more precise. However, they still fail to produce sharp imagery. For example, NeRFlow lacks the details on the leftmost character in the third column in row (c). Furthermore, the second column in row (d) shows blurriness and ghosting

Fig. 7. We show visual results on 4 different synthetic scenes. These scenes include moving characters and dynamic backgrounds. In the above image, each row is rendered using one method from (a) MPI/LLFF [1], (b) 2D Mask, (c) NeRFlow [6], (d) Non-rigid NeRF [8], (e) Neural Scene Flow Field [7], (f) IBRNet [49], and (g) ours. Last row (h) is the ground truth. Our proposed method (g) produces results with fewer artifacts and more temporal stability.

TABLE V
COMPARISON ON THE SYNTHETIC EVALUATION DATASET

Methods	Mask	STRRED↓	PSNR↑	SSIM↑
MPI/LLFF [1]	✗	0.2889	26.12	0.8345
2D Mask	2D	0.5428	24.01	0.8082
IBRNet (2-view) [49]	✗	1.7984	21.37	0.6942
NeRFlow [6]	✗	1.8306	19.99	0.5996
NSFF [7]	✗	1.0627	19.72	0.5577
Non-rigid NeRF [8]	✗	3.1401	18.92	0.5947
Ours	3D	**0.2812**	**26.13**	**0.8342**

artifacts for Non-rigid NeRF. NSFF (e) has issues rendering complex static scene texture in the last column. The table to the left shows distorted edges compared to our proposed method. IBRNet (f) still generates renderings with heavy distortions, even though the coarse geometry seemingly matches the ground truth. Our method (g) provides the best visual result and it is able to generalize to unseen synthetic scenes when trained on real data. Please refer to the supplementary video for more results, available online.

D. Ablation Studies on Loss Function

In this sub-section, we experiment with different losses to see if we can acquire a 3D mask volume that is more interpretable and possesses physical meaning. Two additional loss functions are described as follows. The first loss is a mask supervision loss $\mathcal{L}_m$, which forces the mask volume to match the shape of the dynamic object in the scene. The second loss is a sparsity loss $\mathcal{L}_s$ applied on the mask volume to encourage the network to reuse $\hat{\mathbf{M}}$ more. To be more specific, for the mask loss, we use the work by Lin et al. [46], which takes the individual frame $\mathbf{I}$ and the background $\hat{\mathbf{I}}$ in the video to generate a dynamic object mask $\mathbf{V}_{gt}$ we later use as supervision. To supervise the mask volume, we directly regularize the over-composited alphas from the warped foreground MPI volume $\mathcal{W}(\mathbf{M} \odot \mathbf{V})$ to be consistent with $\mathbf{V}_{gt}$. We denote the over-composited alpha values as m_1. This mask

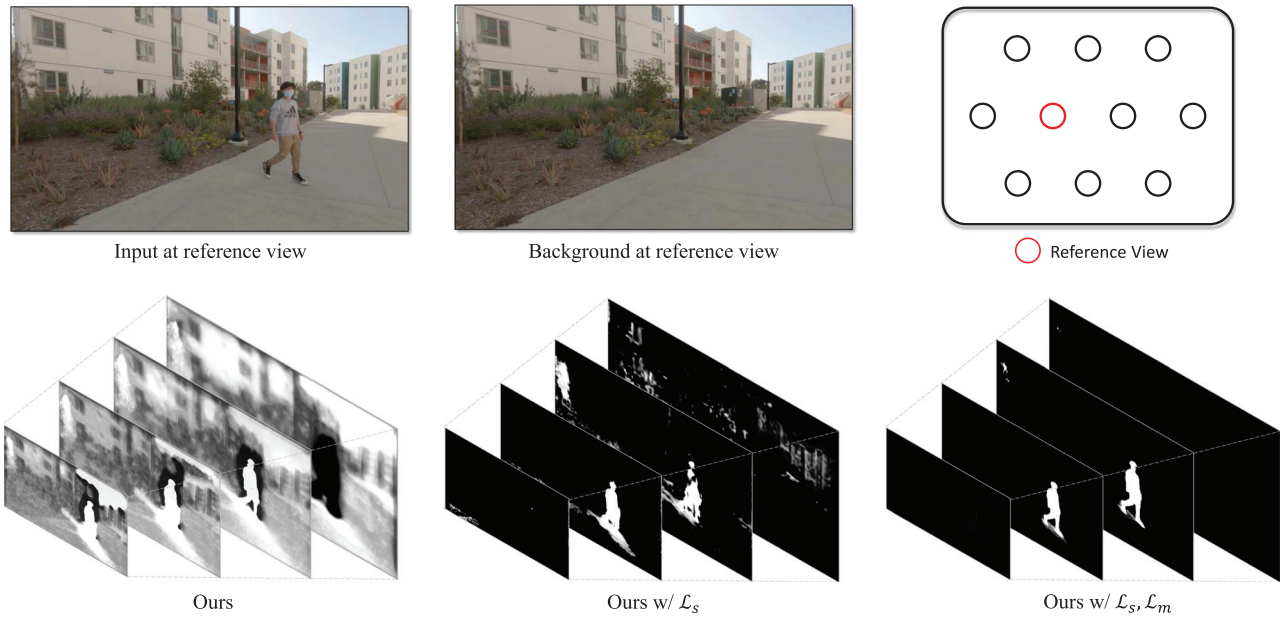

Fig. 8. 3D visualization of the masks from different loss functions. With alpha values from the instantaneous MPI, we collapse the mask volumes using over composite to reduce plane count from 32 to 4 for better visualization. (e.g., plane 1∼8 to the furthest plane,..., plane 25∼32 to the nearest plane.) Note that there is no supervision on static parts in our final loss function, so the values in those parts are unconstrained, resulting in soft blending between instantaneous frames and the background. In general, the 3D mask achieves better temporal consistency by replacing the erroneous disoccluded parts with correct background observations.

TABLE VI
EFFECT OF DIFFERENT LOSS FUNCTIONS

$\mathcal{L}_s$	$\mathcal{L}_m$	STRRED↓	PSNR↑	SSIM↑
-	-	**0.1683**	**26.22**	0.8390
✓	-	0.1745	26.18	**0.8393**
✓	✓	0.1900	26.09	0.8374

Our rendering loss offers better temporal consistency and slightly better visual quality.

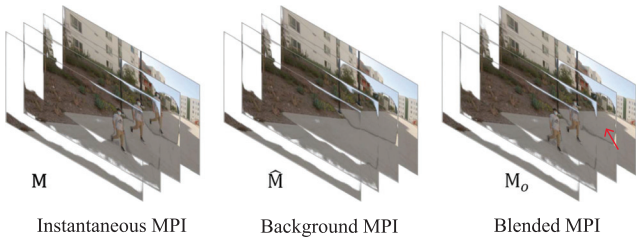

Fig. 9. 3D visualization of the MPI volumes using our loss function $\mathcal{L}$. Note that the person on the furthest plane in $\mathbf{M}$ is replaced by the background in $\mathbf{M}_o$.

loss is similar to the mask supervision loss in Lu et al. [55] We calculate the estimated background mask m_0 by dilating the foreground mask with a kernel of size $(5, 5)$ to produce m_1'. The background mask is then $m_0 = 1 - m_1'$. And the mask supervision loss is

$$\mathcal{L}_m = \frac{||m_1 \odot (1 - \mathbf{V}_{gt})||_1}{2||m_1||_1} + \frac{||m_0 \odot \mathbf{V}_{gt}||_1}{2||m_0||_1}. \quad (12)$$

Another loss is a L_1 sparsity constraint on the mask volume to ensure it only covers the necessary portions,

$$\mathcal{L}_s = || \sum_{(x,y,d)} \mathbf{V}(x, y, d)||_1. \quad (13)$$

We use $\mathcal{L} + 0.1\mathcal{L}_s + 0.25\mathcal{L}_m$ for the full combination and $\mathcal{L} + 0.1\mathcal{L}_s$ for the additional sparsity constraint.

As shown in Table VI, our rendering loss still offers the most temporally-stable results, whereas the other two losses trade temporal consistency for better interpretability. It is reasonable that the mask supervision loss helps the network to give a sparser and tighter prediction on the dynamic objects. However, it does not take into account the movements of the foliage and the shadows, producing slightly unstable results in those areas. The sparsity constraint is able to achieve marginally better quality than the full $\mathcal{L}_s, \mathcal{L}_m$ combination as it retains some parts of the scene which might cover the slight differences between frames.

Mask visualization can be found in Fig. 8. From the figure, we can observe that our mask volume removes areas around the edges of the dynamic object and the occluded areas behind it. Moreover, the mask softly blends the shadows cast by the moving object. Adding $\mathcal{L}_s$, the mask becomes sparser, ignoring most static areas. However, as shown in Fig. 8, it still contains some areas around the plants on the left and the building in the back. With $\mathcal{L}_s, \mathcal{L}_m$, the mask has more physical meaning and the resulting 3D mask only covers the dynamic object. This might be useful to extract moving objects for other uses such as editing or object insertion.

Fig. 10. Our algorithm is able to provide better visual quality than baseline methods even when the novel viewpoint is far away from the input view. We show results when the baseline is 2.5× and 5× baseline between input views. Note that in the 5× case, our method produces fewer artifacts compared to Mildenhall et al. [1], offering a more graceful degradation.

Fig. 11. Our proposed method can also be extended to take 4-view input. We feed 4 input views to both the MPI and mask networks to acquire our result. Here the baseline method is also adjusted to use 4 input views instead of 2. Notice that the artifacts around the person do not appear in our result.

We further examine the 3D visualization of $\mathbf{M}$, $\hat{\mathbf{M}}$, and $\mathbf{M}_o$ in Fig. 9. Note that in the blended MPI $\mathbf{M}_o$, the occluded area behind the person is filled with actual background information, unlike in $\mathbf{M}$, which has repeated texture of the dynamic object. Since we do not enforce any constraints on the static parts of the scene, our mask has random values in these areas and softly blends them with the background MPI. *This does not affect temporal consistency too much as the difference is minor and some areas are free space which does not contribute any color to the MPI volume as shown in Fig. 9.*

E. Large Distance View Extrapolation

In Fig. 10, we show results when the target camera is translated far more than the baseline of the input camera pair. When large translational movement is introduced, the conventional method [1] starts to show artifacts in the disoccluded regions. On the contrary, our method still preserves the background details even when the motion is larger, offering a more graceful reduction in quality as the distance is increased.

F. Extension to More Input Views

Although our proposed method primarily targets binocular view extrapolation, we also demonstrate that it can be extended to utilize more input views in Fig. 11 and in the supplementary video, available online. With more input views, it can acquire better scene geometry for some cases where there are ambiguities in the plane sweep volume. For example, some ambiguities might occur when there is straight texture-less structure (beams or handrails) parallel to the camera baseline. Using additional cameras can provide more geometric information and avoid similar situations. In Fig. 11, the main difference is that we modify our network to take 4 input views, which convert to 4 instantaneous images and 4 background images as input to the

Fig. 12. From top to bottom, we show frame 0, frame 966 (last frame) and the extracted background. Since the lighting changes drastically during this scene, the extracted background contains a lot of ghosting artifacts.

mask network, and output the 3D mask volume as in the pipeline shown in Fig. 4.

G. Limitations

The proposed dataset and algorithm have a few limitations: First, we limit our camera to stay static when capturing. This is mainly due to the limitations of synchronization and pose estimation. Although we can achieve good synchronization with software-based methods, there are still a few milliseconds of error. This error could be magnified when the camera rig is in motion and lead to bad estimates of the camera poses. The camera poses across time would also require more calculations, possibly leading to accumulating errors in the system. These issues could be solved by calibrating the camera trajectory of one of the cameras and utilizing the rigid assumption to infer the trajectories of other cameras. Another limitation is that we require an estimate of the static background. This is easily achievable by applying a median filter. While it works for most of the scenes, this method is sometimes not reliable. We show one example in Fig. 12. In this particular case, the sun light appears after a while in the video, casting hard shadows on the walls. As a result, the background is difficult to determine. Another possible case happens when a static object is moved during the video. It is ambiguous to define the exact background for this case as both states might take up a large portion of the video. Thus, it might require more careful division of different states or using a lighting-agnostic method. There are more advanced approaches [56], [57] that can be used in the future.

VI. Conclusion and Future Work

In this paper, we discuss view synthesis of dynamic scenes with stereo input videos. The main challenge is that rendered results are prone to temporal artifacts like flickering in the disoccluded regions. To tackle this issue, we introduce a novel 3D mask volume extension to carefully replace the disoccluded areas with background information acquired from the temporal frames. Additionally, we introduce a high-quality multi-view video dataset, which contains 96 scenes of various human interactions and outdoor environments shot in 120FPS.

In future work, we would like to extend our dataset and method to consider dynamic camera motions, and to operate on even larger baselines. In summary, we believe video view synthesis for dynamic scenes is the next frontier for immersive applications, and this paper has taken a key step in that direction.

Acknowledgments

We also acknowledge gifts from Adobe, Google, an Amazon Research Award, a Facebook Distinguished Faculty Award, a Sony Research Award, the Ronald L. Graham Chair, and the UC San Diego Center for Visual Computing. Part of the work was done when KEL was an intern at Facebook. Lastly, we thank Jiyang Yu, Yuzhe Qin, Dominique Meyer, Eric Lo, Thomas DeFanti, Jürgen Schulze and Michael Broxton for comments on hardware setup.

References

[1] B. Mildenhall et al., "Local light field fusion: Practical view synthesis with prescriptive sampling guidelines," *ACM Trans. Graph.*, vol. 38, 2019, Art. no. 29.
[2] T. Zhou, R. Tucker, J. Flynn, G. Fyffe, and N. Snavely, "Stereo magnification: Learning view synthesis using multiplane images," *ACM Trans. Graph.*, vol. 37, 2018, Art. no. 65.
[3] P. P. Srinivasan, R. Tucker, J. T. Barron, R. Ramamoorthi, R. Ng, and N. Snavely, "Pushing the boundaries of view extrapolation with multiplane images," in *Proc. IEEE/CVF Conf. Comput. Vis. Pattern Recognit.*, 2019, pp. 175–184.
[4] M.-L. Shih, S.-Y. Su, J. Kopf, and J.-B. Huang, "3D photography using context-aware layered depth inpainting," in *Proc. IEEE Conf. Comput. Vis. Pattern Recognit.*, 2020, pp. 8025–8035.
[5] K.-E. Lin, L. Xiao, F. Liu, G. Yang, and R. Ramamoorthi, "Deep 3D mask volume for view synthesis of dynamic scenes," in *Proc. IEEE/CVF Int. Conf. Comput. Vis.*, 2021, pp. 1729–1738.
[6] Y. Du, Y. Zhang, H.-X. Yu, J. B. Tenenbaum, and J. Wu, "Neural radiance flow for 4D view synthesis and video processing," in *Proc. IEEE/CVF Int. Conf. Comput. Vis.*, 2021, pp. 14304–14314.
[7] Z. Li, S. Niklaus, N. Snavely, and O. Wang, "Neural scene flow fields for space-time view synthesis of dynamic scenes," in *Proc. IEEE/CVF Conf. Comput. Vis. Pattern Recognit.*, 2021, pp. 6494–6504.
[8] E. Tretschk, A. Tewari, V. Golyanik, M. Zollhöfer, C. Lassner, and C. Theobalt, "Non-rigid neural radiance fields: Reconstruction and novel view synthesis of a dynamic scene from monocular video," in *Proc. IEEE Int. Conf. Comput. Vis.*, 2021, pp. 12939–12950.
[9] J. Flynn et al., "DeepView: View synthesis with learned gradient descent," in *Proc. IEEE/CVF Conf. Comput. Vis. Pattern Recognit.*, 2019, pp. 2367–2376.
[10] M. Broxton et al., "Immersive light field video with a layered mesh representation," *ACM Trans. Graph.*, vol. 39, no. 4, pp. 86:1–86:15, 2020.
[11] J. S. Yoon, K. Kim, O. Gallo, H. S. Park, and J. Kautz, "Novel view synthesis of dynamic scenes with globally coherent depths from a monocular camera," in *Proc. IEEE/CVF Conf. Comput. Vis. Pattern Recognit.*, 2020, pp. 5336–5345.
[12] Q. Li and N. Khademi Kalantari, "Synthesizing light field from a single image with variable MPI and two network fusion," *ACM Trans. Graph.*, vol. 39, no. 6, Dec. 2020, Art. no. 229.
[13] A. Bansal, M. Vo, Y. Sheikh, D. Ramanan, and S. Narasimhan, "4D visualization of dynamic events from unconstrained multi-view videos," in *Proc. IEEE/CVF Conf. Comput. Vis. Pattern Recognit.*, 2020, pp. 5366–5375.
[14] Z. Li et al., "Learning the depths of moving people by watching frozen people," in *Proc. IEEE/CVF Conf. Comput. Vis. Pattern Recognit.*, 2019, pp. 4521–4530.
[15] M. Bemana, K. Myszkowski, H.-P. Seidel, and T. Ritschel, "X-Fields: Implicit neural view-, light- and time-image interpolation," *ACM Trans. Graph.*, vol. 39, no. 6, 2020, Art. no. 257.
[16] M. Menze and A. Geiger, "Object scene flow for autonomous vehicles," in *Proc. IEEE Conf. Comput. Vis. Pattern Recognit.*, 2015, pp. 3061–3070.
[17] S. J. Gortler, R. Grzeszczuk, R. Szeliski, and M. F. Cohen, "The lumigraph," in *Proc. 23rd Annu. Conf. Comput. Graph. Interactive Techn.*, 1996, pp. 43–54.
[18] M. Levoy and P. Hanrahan, "Light field rendering," in *Proc. 23rd Annu. Conf. Comput. Graph. Interactive Techn.*, 1996, pp. 31–42.
[19] C. Buehler, M. Bosse, L. McMillan, S. Gortler, and M. Cohen, "Unstructured lumigraph rendering," in *Proc. 28th Annu. Conf. Comput. Graph. Interactive Techn.*, 2001, pp. 425–432.

[20] P. E. Debevec, C. J. Taylor, and J. Malik, "Modeling and rendering architecture from photographs: A hybrid geometry-and image-based approach," in *Proc. 23rd Annu. Conf. Comput. Graph. Interactive Techn.*, 1996, pp. 11–20.
[21] J. Shade, S. Gortler, L.-W. He, and R. Szeliski, "Layered depth images," in *Proc. 25th Annu. Conf. Comput. Graph. Interactive Techn.*, 1998, pp. 231–242.
[22] A. Davis, M. Levoy, and F. Durand, "Unstructured light fields," *Comput. Graph. Forum*, vol. 31, no. 2pt1, pp. 305–314, 2012.
[23] E. Penner and L. Zhang, "Soft 3D reconstruction for view synthesis," *ACM Trans. Graph.*, vol. 36, no. 6, pp. 1–11, 2017.
[24] P. Hedman, J. Philip, T. Price, J.-M. Frahm, G. Drettakis, and G. Brostow, "Deep blending for free-viewpoint image-based rendering," *ACM Trans. Graph.*, vol. 37, no. 6, pp. 1–15, 2018.
[25] J. Flynn, I. Neulander, J. Philbin, and N. Snavely, "Deep stereo: Learning to predict new views from the world's imagery," in *Proc. IEEE Conf. Comput. Vis. Pattern Recognit.*, 2016, pp. 5515–5524.
[26] N. K. Kalantari, T.-C. Wang, and R. Ramamoorthi, "Learning-based view synthesis for light field cameras," *ACM Trans. Graph.*, vol. 35, no. 6, pp. 1–10, 2016.
[27] Z. Xu, S. Bi, K. Sunkavalli, S. Hadap, H. Su, and R. Ramamoorthi, "Deep view synthesis from sparse photometric images," *ACM Trans. Graph.*, vol. 38, no. 4, Jul. 2019, Art. no. 76. [Online]. Available: https://doi.org/10.1145/3306346.3323007
[28] S. Niklaus, L. Mai, J. Yang, and F. Liu, "3D Ken burns effect from a single image," *ACM Trans. Graph.*, vol. 38, no. 6, pp. 1–15, 2019.
[29] B. Mildenhall, P. P. Srinivasan, M. Tancik, J. T. Barron, R. Ramamoorthi, and R. Ng, "NeRF: Representing scenes as neural radiance fields for view synthesis," in *Proc. Eur. Conf. Comput. Vis.*, Springer, 2020, pp. 405–421.
[30] C. Jiang et al., "Local implicit grid representations for 3D scenes," in *Proc. IEEE/CVF Conf. Comput. Vis. Pattern Recognit.*, 2020, pp. 6001–6010.
[31] S. Lombardi, T. Simon, J. Saragih, G. Schwartz, A. Lehrmann, and Y. Sheikh, "Neural volumes: Learning dynamic renderable volumes from images," 2019, *arXiv:1906.07751*.
[32] V. Sitzmann, J. Thies, F. Heide, M. Nießner, G. Wetzstein, and M. Zollhofer, "DeepVoxels: Learning persistent 3D feature embeddings," in *Proc. IEEE/CVF Conf. Comput. Vis. Pattern Recognit.*, 2019, pp. 2437–2446.
[33] J. J. Park, P. Florence, J. Straub, R. Newcombe, and S. Lovegrove, "DeepSDF: Learning continuous signed distance functions for shape representation," in *Proc. IEEE/CVF Conf. Comput. Vis. Pattern Recognit.*, 2019, pp. 165–174.
[34] K.-E. Lin et al., "Deep multi depth panoramas for view synthesis," in *Proc. Eur. Conf. Comput. Vis.*, 2020, pp. 328–344.
[35] R. Szeliski and P. Golland, "Stereo matching with transparency and matting," in *Proc. 6th Int. Conf. Comput. Vis.*, 1998, pp. 517–524.
[36] Z. Xu, K. Sunkavalli, S. Hadap, and R. Ramamoorthi, "Deep image-based relighting from optimal sparse samples," *ACM Trans. Graph.*, vol. 37, no. 4, Jul. 2018, Art. no. 126. [Online]. Available: https://doi.org/10.1145/3197517.3201313
[37] S. Bi et al., "Deep reflectance volumes: Relightable reconstructions from multi-view photometric images," 2020, *arXiv:2007.09892*.
[38] S. Bi et al., "Neural reflectance fields for appearance acquisition," 2020, *arXiv:2008.03824*.
[39] M. Meshry et al., "Neural rerendering in the wild," in *Proc. IEEE/CVF Conf. Comput. Vis. Pattern Recognit.*, 2019, pp. 6878–6887.
[40] C. L. Zitnick, S. B. Kang, M. Uyttendaele, S. Winder, and R. Szeliski, "High-quality video view interpolation using a layered representation," *ACM Trans. Graph.*, vol. 23, no. 3, pp. 600–608, 2004.
[41] D. A. Forsyth and J. Ponce, *Computer Vision: A Modern Approach*. Hoboken, NJ, USA: Prentice Hall Professional Technical Reference, 2002.
[42] G. Bradski, "The OpenCV library," *Dr Dobb's J. Softw. Tools*, vol. 120, pp. 122–125, 2000.
[43] J. L. Schönberger, E. Zheng, M. Pollefeys, and J.-M. Frahm, "Pixelwise view selection for unstructured multi-view stereo," in *Proc. Eur. Conf. Comput. Vis.*, 2016, pp. 501–518.
[44] J. L. Schönberger and J.-M. Frahm, "Structure-from-motion revisited," in *Proc. IEEE Conf. Comput. Vis. Pattern Recognit.*, 2016, pp. 4104–4113.
[45] R. Szeliski and P. Golland, "Stereo matching with transparency and matting," *Int. J. Comput. Vis.*, vol. 32, no. 1, pp. 45–61, 1999.
[46] S. Lin, A. Ryabtsev, S. Sengupta, B. Curless, S. Seitz, and I. Kemelmacher-Shlizerman, "Real-time high-resolution background matting," 2020, *arXiv:2012.07810*.
[47] K. Simonyan and A. Zisserman, "Very deep convolutional networks for large-scale image recognition," 2014, *arXiv:1409.1556*.
[48] Q. Chen and V. Koltun, "Photographic image synthesis with cascaded refinement networks," in *Proc. IEEE Int. Conf. Comput. Vis.*, 2017, pp. 1511–1520.
[49] Q. Wang et al., "IBRNet: Learning multi-view image-based rendering," in *Proc. IEEE/CVF Conf. Comput. Vis. Pattern Recognit.*, 2021, pp. 4688–4697.
[50] A. Paszke et al., "PyTorch: An imperative style, high-performance deep learning library," in *Proc. Adv. Neural Inf. Process. Syst.*, H. Wallach, H. Larochelle, A. Beygelzimer, F. D. Alché-Buc, E. Fox, and R. Garnett, Eds., Curran Associates, Inc., 2019, pp. 8024–8035. [Online]. Available: http://papers.neurips.cc/paper/9015-pytorch-an-imperative-style-high-performance-deep-learning-library.pdf
[51] R. Soundararajan and A. C. Bovik, "Video quality assessment by reduced reference spatio-temporal entropic differencing," *IEEE Trans. Circuits Syst. Video Technol.*, vol. 23, no. 4, pp. 684–694, Apr. 2013.
[52] S. K. Ramakrishnan et al., "Habitat-matterport 3D dataset (HM3D): 1000 large-scale 3D environments for embodied AI," in *Proc. 35th Conf. Neural Inf. Process. Syst. Datasets Benchmarks Track*, 2021.
[53] E. Games, "Unreal engine sun temple, open research content archive (ORCA)," Oct. 2017. [Online]. Available: http://developer.nvidia.com/orca/epic-games-sun-temple
[54] Blender Online Community, "Blender - A 3D modelling and rendering package, blender foundation," Blender Institute, Amsterdam, 2020. [Online]. Available: http://www.blender.org
[55] E. Lu et al., "Layered neural rendering for retiming people in video," *ACM Trans. Graph.*, vol. 39, no. 6, Nov. 2020, Art. no. 256. [Online]. Available: https://doi.org/10.1145/3414685.3417760
[56] J. He, L. Balzano, and A. Szlam, "Incremental gradient on the grassmannian for online foreground and background separation in subsampled video," in *Proc. IEEE Conf. Comput. Vis. Pattern Recognit.*, 2012, pp. 1568–1575.
[57] S. Hauberg, A. Feragen, and M. J. Black, "Grassmann averages for scalable robust PCA," in *Proc. IEEE Conf. Comput. Vis. Pattern Recognit.*, 2014, pp. 3810–3817.

Kai-En Lin received the BSc degree in electrical engineering from National Taiwan University, Taiwan. He is currently working toward the PhD degree with the Department of Computer Science, University of California, San Diego. His research interests focus on view synthesis, specifically 3D representations from single or multiple images.

Guowei Yang received the bachelor's degree in EECS from UC Berkeley, in 2019. He then did a 7 months internship with Apple, focusing on visual computing projects. From 2020 to 2022, he is currently working toward the master's degree with UC San Diego. He was also working as a graduate student researcher in prof. Ravi Ramamoorthi's lab, focusing on view synthesis problems. His research interests are computer vision and graphics. Currently, he is a research engineer with Apple on the Camera Algorithm team.

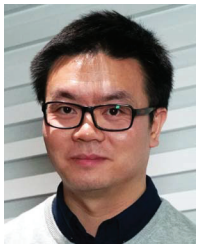

Lei Xiao received the PhD degree in computer science from the University of British Columbia. He is a research scientist with Reality Labs Research, Meta. His recent research focuses on neural rendering and its applications to virtual reality, mixed reality, and computational photography.

Feng Liu received the BE and ME degrees in computer science from Zhejiang University, in 2001 and 2004, respectively, and the MS and PhD degrees in computer science from the University of Wisconsin, Madison, in 2006 and 2010, respectively. He is an Associate Professor with the Department of Computer Science, Portland State University. His research interests are in the areas of computer vision, computer graphics, and multimedia. He was a visiting researcher with Google from 2017–2018 and with Facebook from 2020–2021.

Ravi Ramamoorthi (Fellow, IEEE) received the BS degree in engineering and applied science and MS degrees in computer science and physics from the California Institute of Technology, in 1998, and the PhD degree in computer science from the Stanford University Computer Graphics Laboratory, in 2002, upon which he joined the Columbia University Computer Science Department. He was on the UC Berkeley EECS faculty from 2009–2014. Since, July 2014, he is a professor of computer science and engineering with the University of California, San Diego, where he holds the Ronald L. Graham chair of computer science. He is also the founding director of the UC San Diego Center for Visual Computing. His research interests cover many areas of computer vision and graphics, with more than 200 publications. His research has been recognized with a number of awards, including the 2007 ACM SIGGRAPH Significant New Researcher Award in computer graphics, and by the white house with a Presidential Early Career Award for Scientists and Engineers, in 2008 for his work on physics-based computer vision. Most recently, he was named an ACM fellow, in 2017, and inducted into the SIGGRAPH Academy, in 2019. He has advised more than 20 postdoctoral, PhD and MS students, many of whom have gone on to leading positions in industry and academia; and he has taught the first open online course in computer graphics on the edX platform in fall 2012, with more than 100,000 students enrolled in that and subsequent iterations. He was a finalist for the inaugural 2016 edX Prize for exceptional contributions in online teaching and learning, and again, in 2017.